IOP Publishing Nano Futures 6 (2022) 025007 https://doi.org/10.1088/2399-1984/ac7098

NANO FUTURES

PAPER

# Enhanced water oxidation reaction activity of $Mn_3O_4$ nanocrystals in an alkaline medium by doping transition-metal ions

P Saraswathi[2], Anjaly Babu[3], S D Ramarao[1,*], K Uday Kumar[3], Hitesh Borkar[3], Ch Rajesh[4] and K Raghavendra Kumar[2]

[1] Department of Humanities and Sciences (Physics), VNR Vignana Jyothi Institute of Engineering and Technology, Hyderabad, Telangana 500 090, India
[2] Department of Physics, Koneru Lakshmaiah Education Foundation, Vaddeswaram, Andhra Pradesh 522 502, India
[3] Energy Materials and Devices Laboratory, Department of Physics, National Institute of Technology, Warangal, Telangana 506 004, India
[4] Department of Physics, GVP College of Engineering (A), Madhurawada, Visakhapatnam, Andhra Pradesh 530 048, India
[*] Author to whom any correspondence should be addressed.

**E-mail:** dasaradh4phy@gmail.com **and** dasaradharamarao_s@vnrvjiet.in

**Keywords:** spinel structure, electrocatalyst, alkaline medium, oxygen evolution reaction, turnover frequency, Tafel slope

**RECEIVED**
10 March 2022

**REVISED**
11 May 2022

**ACCEPTED FOR PUBLICATION**
16 May 2022

**PUBLISHED**
20 June 2022

## Abstract

Designing low-cost, Earth-abundant, and non-precious catalysts for electrochemical water oxidation reactions is particularly important for accelerating the development of sustainable energy sources and, further, can be fed to fuel cells. In the present work, we report the oxygen evolution reaction (OER) activity of a metal-oxide catalyst, $Mn_3O_4$, and study the effect of transition metal doping (Cu and Fe) on the OER activity of $Mn_3O_4$ in an alkaline medium. The $Mn_3O_4$ and transition metal (Cu and Fe) doped $Mn_3O_4$ catalysts were prepared using a hydrothermal reaction technique. Powder x-ray diffraction studies revealed that these compounds adopt a tetragonal spinel structure with an $I4_1/amd$ space group, and this is further supported with Fourier transform infrared spectroscopic measurements. These results are further supported by high-resolution transmission electron microscopic measurements. The electrochemical measurements of these catalysts reveal that the transition metal (Cu and Fe) doped $Mn_3O_4$ catalysts show better OER activity than pristine $Mn_3O_4$ (MO). The transition metal (Cu and Fe) doped $Mn_3O_4$ catalysts exhibit lower overpotential for the OER ($\eta_{MCO} = 300$ mV and $\eta_{MFO} = 240$ mV) than the MO ($\eta_{MO} = 350$ mV) catalyst. The better performance of Fe-doped $Mn_3O_4$ is further supported by turnover frequency calculations.

## List of abbreviations

| | |
|---|---|
| CV | cyclic voltametry |
| ECSA | electrochemical active surface area |
| EDS | energy dispersive x-ray spectroscopy |
| FESEM | field emission scanning electron microscope |
| FTIR | Fourier transform infrared |
| HRTEM | high-resolution transmission electron microscope |
| LDHs | layered double hydroxides |
| LSV | linear sweep voltammetry |
| MCO | Cu-doped $Mn_3O_4$ |
| MFO | Fe-doped $Mn_3O_4$ |
| MO | pristine metal oxide, $Mn_3O_4$ |
| OER | oxygen evolution reaction |
| PXRD | powder x-ray diffraction |
| RHE | reversible hydrogen electrode |
| TEM | transmission electron microscope |
| TOF | turnover frequency |

## 1. Introduction

Increasing population and globalization demand the generation of a huge amount of energy, and most of this energy is produced through burning fossil fuels [1–3]. The continuous burning of fossil fuels leads to significant environmental issues [3]. Apart from this, the depletion of fossil fuels is another major concern, which requires identifying alternative and renewable energy sources [4, 5]. The generation and storage of clean energy with the help of fuel cells [6, 7], electrolyzers [8, 9], and metal-air batteries [10, 11] is an emerging area that many researchers are currently investigating. The oxygen evolution reaction (OER) plays a crucial role in many electrochemical processes that are taking place in energy conversion and storage technologies [12, 13]. Currently, precious, noble metal-based oxides such as $IrO_2$ and $RuO_2$ are used as OER catalysts in electrolyzing devices [14]. Despite excellent OER activity, these state-of-the-art catalysts restrict the commercialization of technologies due to their huge cost and low Earth-abundance. This has triggered researchers to design cheap and more abundant OER catalysts [15].

Recently, non-precious metal oxide-based catalysts have gained a lot of attention in the field of catalysis, energy-storage devices, water splitting [16], and sensors due to their excellent physical and chemical properties [15]. In this direction, many researchers have investigated the electrochemical properties of Mn-, Fe-, and Co-based binary and ternary oxides [17–19]. Apart from these transition metal oxides, layered double hydroxides (LDHs) containing 3d transition metals (Ni, Co, Fe, and Mn) have been reported to exhibit excellent OER activity in an alkaline medium [20, 21]. Among these transition metal oxides and LDHs, Mn-based binary and ternary oxides have attracted the electrochemical scientific community owing to their Earth-abundance and environmentally friendly nature. Manganese (Mn) is an interesting element with a rich redox chemistry and has been observed to acquire multiple oxidation states [22]. Due to this, Mn-based oxides were reported to adopt different crystal structures including, MnO, $Mn_2O_3$, $Mn_3O_4$, $MnO_2$, and $Mn_5O_8$ compounds [22].

The compound $Mn_3O_4$ is found in nature as a Hausmannite mineral and possesses a tetragonal spinel structure with an $I4_1/amd$ space group [23]. In the crystal structure, the Mn exists in a mixed ($Mn^{2+}$ and $Mn^{3+}$) valence state where the $Mn^{2+}$ ions will occupy the tetrahedral sites and the octahedral sites are filled with $Mn^{3+}$ ions [24]. The mixed valent $Mn_3O_4$ compound has attracted the scientific community because of its potential applications in supercapacitors [25], Li-ion batteries [26], energy storage [27], gas-sensing [28], and targeted drug delivery [29]. The compound $Mn_3O_4$ shows good stability in an alkaline medium and is well explored for OER applications [30–32]. It was reported that the OER activity of $Mn_3O_4$ was observed to enhance with the incorporation of noble metals [33, 34]. To avoid the use of precious noble metals and enhance the OER activity of $Mn_3O_4$, researchers reported several strategies, such as using different synthesis techniques [35], doping [36, 37], and forming heterostructures [38–40], hierarchical core–shell nanostructures [41–43], and nanocomposites [39]. Apart from these, tailoring morphology and producing nanocrystals of these metal oxide catalysts was another important strategy to enhance the catalytic activity due to exposure of different crystallographic planes over which different catalytic reactions can occur [44–46].

To the best of our knowledge, no reports were found on the electrochemical OER activity of transition metal (Cu and Fe) doped $Mn_3O_4$ nanocrystals in an alkaline medium. Herein, we report the OER activity of Cu-doped $Mn_3O_4$ (MCO) and Fe-doped $Mn_3O_4$ (MFO) and compare these results with the pristine metal oxide $Mn_3O_4$ (MO). It was found that the doping of transition-metal (Cu and Fe) ions enhances the OER activity of $Mn_3O_4$.

## 2. Experimental procedure

### 2.1. Synthesis of $Mn_3O_4$ and transition metal-modified $Mn_3O_4$ using a hydrothermal method

The nanocrystals of $Mn_3O_4$ and transition metal (Cu and Fe) doped $Mn_3O_4$ were synthesized by a hydrothermal method. In a typical synthesis procedure of $Mn_3O_4$, 7.2 mmol of $KMnO_4$ was dissolved in 60 ml of deionized water at room temperature. While stirring, 0.46 mmol of glucose was added gradually to the solution. Here, the glucose acts as a mild reducing agent. The suspension turned brown in colour and was stirred continuously for 40 min. The mixture was transferred into a 100 ml capacity Teflon-lined autoclave.

To synthesize transition metal (Cu and Fe) doped $Mn_3O_4$, the corresponding metal sulphates were introduced into the brown coloured suspension obtained in the previous procedure. The molar ratio between the Mn and the transition metals (Cu and Fe) was maintained at 1:0.05. The resultant mixture was stirred for another 30 min and was then transferred into a 100 ml capacity Teflon-lined autoclave. These autoclaves were heated in an oven that was maintained at 200 °C for 2 h. After the hydrothermal process, the autoclaves were allowed to cool naturally. The resulting solid product was filtered, washed with distilled water and ethanol, and finally dried at 70 °C for 14 h.

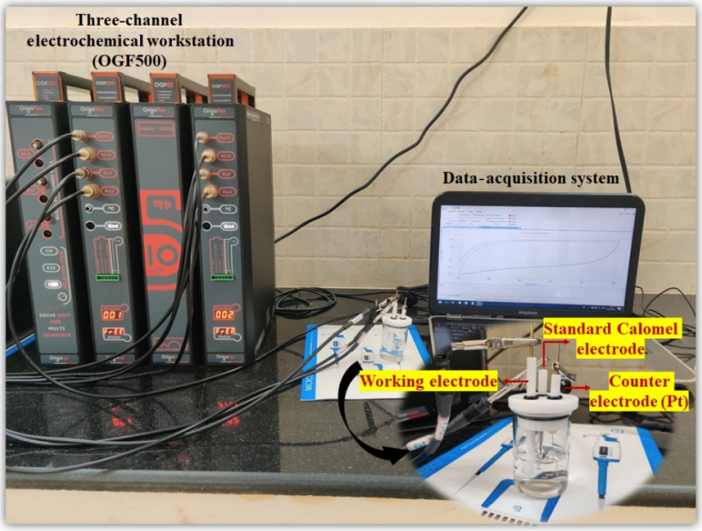


**Figure 1.** Experimental setup for performing the OER on a transition metal-doped $Mn_3O_4$ catalyst.

## 3. Characterization

Powder x-ray diffraction (PXRD) measurements were done on the as-synthesized and transition metal (Cu and Fe) doped $Mn_3O_4$ compounds with the help of a PANalytical X'pert Pro diffractometer with Cu–$K_\alpha$ radiation. The phase purity of the as-prepared samples was verified by comparing them with the standard $Mn_3O_4$ compound. The structural features of the as-prepared catalysts were further analyzed with the help of the Fourier transform infrared (FTIR) spectroscopy technique. The data was collected in the range 400–4000 $cm^{-1}$ and an FTIR Bruker Alpha II instrument was used for these measurements. The morphology of the transition metal-modified $Mn_3O_4$ nanocrystals was studied with the help of a field emission scanning electron microscope (FESEM; Zeiss Gemini 500) with an energy dispersive x-ray spectroscopy (EDS) unit. To understand the distribution of elements, elemental mapping was done on all the compounds. A transmission electron microscope (TEM; JEOL JEM-2100) was used to understand the shape of the nanocrystals. To further corroborate the results obtained from PXRD, high-resolution transmission electron micrographs of the compounds were collected.

Electrochemical measurements were done with the help of a three-channel electrochemical workstation (OGF500, Origalys, France), as shown in figure 1. A 0.1 M KOH was used as an electrolyte for these measurements. The glassy carbon working electrodes were coated with catalyst ink, which was prepared by dispersing 2.4 mg of catalyst and 0.6 mg of activated carbon powder (TIMCAL SUPER C65 nano carbon black) in deionized water, isopropanol, and Nafion ionomer solution (5 wt%) (v/v/v = 2.85:0.95:0.20) to form a 400 $\mu$l suspension. Before coating on the working electrode, the catalyst ink was ultrasonicated for 30 min. The catalyst ink (10 $\mu$l) was drop cast onto the glassy carbon electrodes and was allowed to dry overnight. The potentials observed with respect to Ag/AgCl were converted with respect to a reversible hydrogen electrode (RHE) with the help of the equation $E_{RHE} = (0.059 \times pH) + E_{Ag/AgCl} + E_{obs}$. The water oxidation overpotential of the catalysts was calculated by using observed onset potential and the standard water oxidation potential, $\eta = E_{RHE} - 1.23$ V.

The electrochemical active surface area (ECSA) of the catalysts was calculated by performing cyclic voltammetry measurements at different (10, 20, 30, 40, 50, 60, 70, 80, 90, 100) scan rates in the non-faradaic region of 0.10 V–0.60 V vs RHE. In the non-faradaic region, the observed current response is due to the charging of a double layer. The capacitance of this double layer was found by plotting a graph at 0.35 V vs RHE, between $\Delta I$ i.e. $(i_a - i_c)$ and the scan rate, where $i_a$ and $i_c$ represent the anodic and cathodic current, respectively. The slope of this graph gives the double-layer capacitance ($C_{dl}$). Then, the ECSA was calculated with the expression

$$\mathrm{ECSA} = \frac{C_{dl}}{C_s}, \tag{1}$$

where $C_{dl}$ is the double-layer capacitance and $C_s$ represents the capacitance of the catalyst with an ideal flat surface, which is considered 0.04 mF $cm^{-2}$ for manganese-based catalysts [47]. Turnover frequency (TOF) is

another important parameter of an electrocatalyst, which gives the intrinsic activity of the catalysts [48]. The TOFs of all the catalysts were calculated with the help of the expression

$$\mathrm{TOF} = \frac{i}{4nF}, \tag{2}$$

where $I$ and $F$ are current (in A) at a given potential ($E = 1.58$ vs RHE) and the Faraday's constant (96 485 C $mol^{-1}$). Here, $n$ represents the number of active sites on which the OER reaction is occurring and can be calculated with the expression

$$n = \frac{Q}{2F}, \tag{3}$$

where $Q$ is the volumetric charge, which can be obtained by integrating the cyclic voltammetry (CV) curves of the catalysts collected at a 10 mV $s^{-1}$ scan rate [49].

## 4. Results and discussion

### 4.1. Structural and morphology studies

Figure 2 shows the PXRD patterns of the as-synthesized $Mn_3O_4$ and transition metal ion (Cu and Fe) modified $Mn_3O_4$. It was observed that these patterns match with standard $Mn_3O_4$, having a tetragonal structure with an $I4_1/amd$ space group. No extra reflections were observed and it was confirmed that the as-prepared catalysts were of a pure phase. The lattice parameters of MO were obtained with the help of CELREF software and were found to be in the range of $a = b = 5.72$ Å, $c = 9.40$ Å. The substitution of transition elements leads to the expansion of the lattice and can be understood clearly with the observed lattice parameters of MCO ($a = b = 5.76$ Å, $c = 9.42$ Å) and MFO ($a = b = 5.79$ Å, $c = 9.45$ Å). Apart from this, no shift in the high-intensity reflections was observed in the PXRD patterns. Similar results were reported for Ni-, Cr-, and Co-substituted $Mn_3O_4$ [25, 36, 50, 51]. These results suggest that the substituted metal ions (Cu or Fe) replace the $Mn^{2+}$ in the MO catalysts. The substitution is feasible due to the comparable ionic radius of $Cu^{2+}$ (0.73 Å) and $Fe^{2+}$ (0.78 Å) with $Mn^{2+}$ (0.80 Å) [52].

The average crystallite size of the as-prepared catalysts was calculated with the help of the Debye-Scherrer formula [53], as given below:

$$D = \frac{0.94\lambda}{\beta \cos\theta}, \tag{4}$$

where $\lambda$ represents the wavelength of incident x-rays, and $\beta$ and $\theta$ represent the full width at half maxima and the diffraction angle of the high-intensity reflection of the as-prepared catalysts. It is found that the average crystallite size of these catalysts is in the range of 30–50 nm. These results are further supported with microscopic studies of these catalysts. To further understand the formation of the as-synthesized catalysts in the spinel structure, we collected the FTIR spectra, which are shown in figure 3. The modes observed at around 3380 $cm^{-1}$ and 1629 $cm^{-1}$ can be attributed to the stretching and deformational vibrations of hydroxyl groups. The characteristic modes corresponding to Mn–O in the octahedral and tetrahedral sites are observed in the range of 630–480 $cm^{-1}$ and further confirm the phase purity of the as-synthesized catalysts. These results are in line with the literature [54, 55].

Figure 4 shows FESEM micrographs of the MO, MCO, and MFO catalysts. These micrographs indicate that the catalysts have a cubical morphology and are in the range of 50 nm. To further examine the uniform distribution of elements within the as-prepared catalysts, elemental mapping was done and is shown in figure 5. These colour-mapping images confirm the presence of transition metals (Cu, Fe, and Mn) along with oxygen in the MO and modified $Mn_3O_4$ catalysts.

Further investigations were conducted to understand the shape and size of the as-prepared catalyst particles with the help of a TEM, and the corresponding micrographs are shown in figures 6(a)–(c). These micrographs reveal that the shape of the catalyst particles is cubical and the size of these particles is in the range of 50 nm. The results are consistent with the average crystallite size calculated from the Debye-Scherrer formula.

Figures 6(d)–(f) show the high-resolution TEM (HRTEM) images of MO and transition metal (Cu and Fe) doped $Mn_3O_4$ catalysts. These micrographs reveal clear fringes and the corresponding $d$-spacing values are noted. The $d$-spacing of MO was found to be in the range of 0.491 nm and transition metal (Cu and Fe) doped $Mn_3O_4$ shows very close $d$-spacing values, suggesting the substitution of the transition-metal ions ($Cu^{2+}$ and $Fe^{2+}$) at tetrahedral $Mn^{2+}$ sites of $Mn_3O_4$. Similar morphological features were reported by Dong *et al* in transition metal-doped $Mn_3O_4$ compounds [25]. The observed $d$-spacing values corroborate well with the (101) reflection seen in the PXRD data of $Mn_3O_4$.

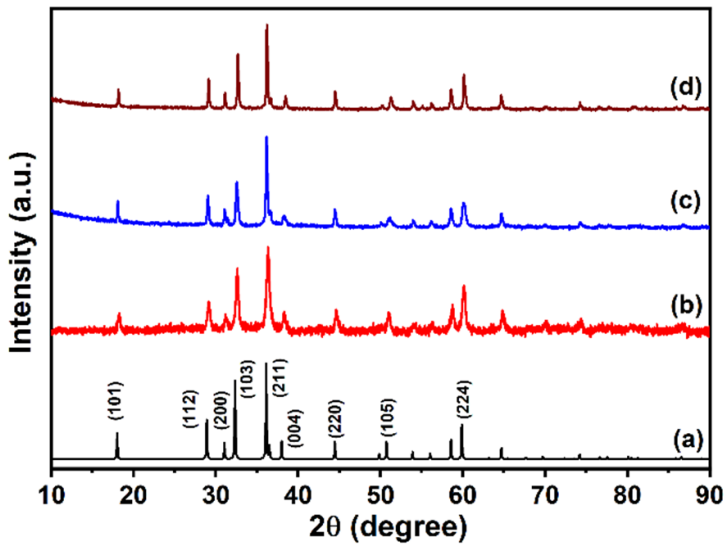


**Figure 2.** Powder x-ray diffraction patterns of (a) standard $Mn_3O_4$, (b) pristine $Mn_3O_4$, (c) Cu-doped $Mn_3O_4$, and (d) Fe-doped $Mn_3O_4$.

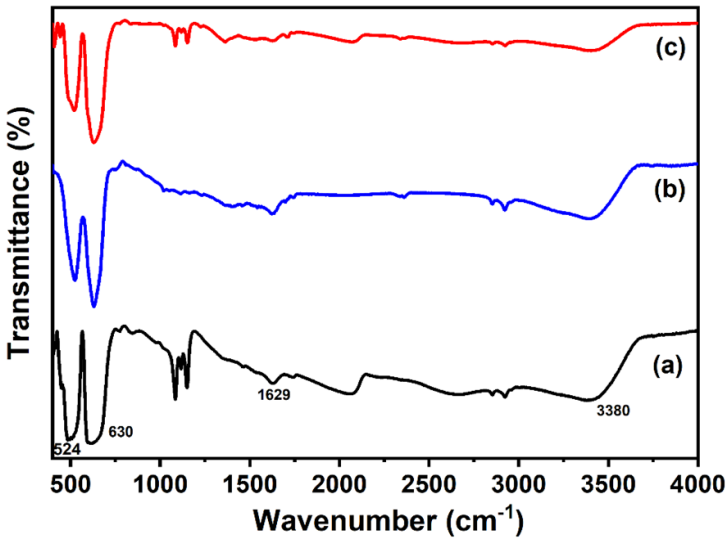


**Figure 3.** FTIR spectra of (a) pristine $Mn_3O_4$, (b) Cu-doped $Mn_3O_4$, and (c) Fe-doped $Mn_3O_4$.

### 4.2. Electrochemical OER studies

The applicability of the as-synthesized catalysts towards water oxidation reaction applications was investigated by performing linear sweep voltammetry (LSV) on the MO and transition metal (Cu and Fe) doped $Mn_3O_4$ catalysts. These electrochemical OERs were done at room temperature in a 0.1 M KOH solution. Figure 7(a) shows the LSV curves of the MO, MCO, and MFO catalysts collected in the range of 1.0–1.9 V vs RHE. It is observed from figure 7(a) that MO shows an onset potential of 1.58 V vs RHE, whereas the MCO and MFO showed a lower onset potential of 1.53 V and 1.47 V vs RHE, respectively, for the OER. The overpotential ($\eta$) of these catalysts is calculated using the following equation:

$$\eta = E_{\mathrm{RHE}} - 1.23\ \mathrm{V}, \tag{5}$$

where $E_{\mathrm{RHE}}$ is the observed onset potential of the catalyst and 1.23 V is the standard water oxidation potential. The calculated overpotential of MO, MCO, and MFO are given in figure 7(a). The observed overpotential of MO ($\eta_{\mathrm{MO}} = 350$ mV) is found to be lower than the reported overpotential values of $Mn_3O_4$ [30, 36, 56]. The transition metal (Cu and Fe) doped $Mn_3O_4$ catalysts show slightly lower overpotential ($\eta_{\mathrm{MCO}} = 300$ mV and $\eta_{\mathrm{MFO}} = 240$ mV) than the MO. Among these catalysts, MFO shows the best catalytic activity towards the water oxidation reaction with an overpotential of $\eta_{\mathrm{MFO}} = 240$ mV. This enhanced

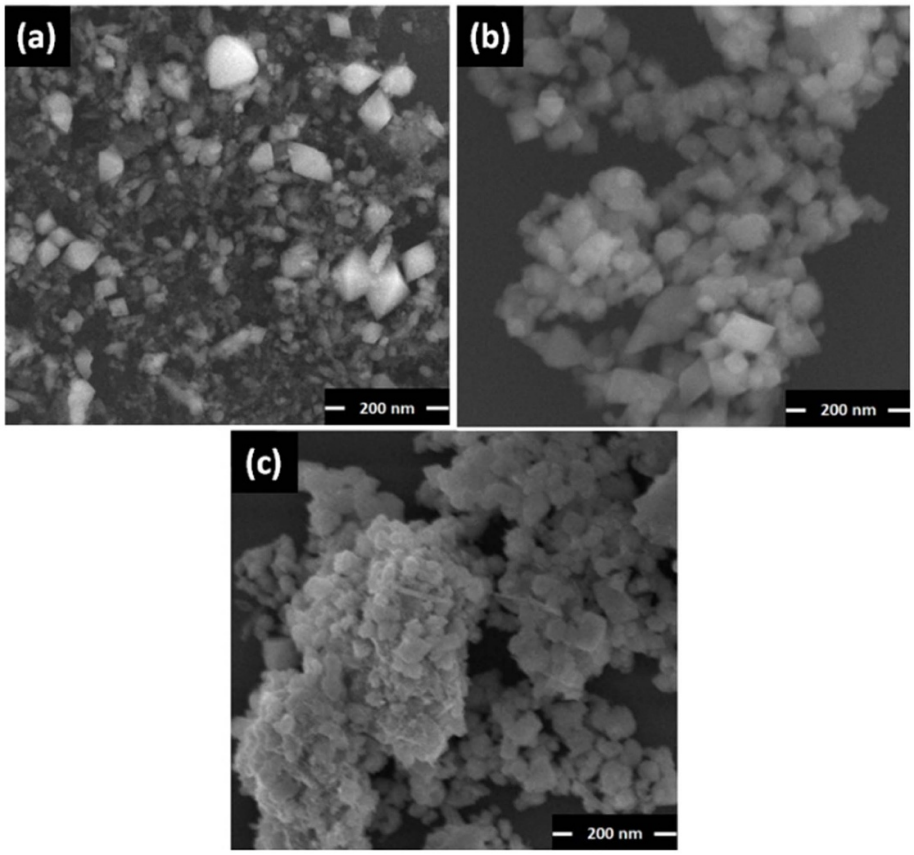


**Figure 4.** FESEM micrographs of as-synthesized (a) pristine $Mn_3O_4$, (b) Cu-doped $Mn_3O_4$, and (c) Fe-doped $Mn_3O_4$ catalysts.

activity of transition metal (Cu and Fe) doped $Mn_3O_4$ catalysts could be attributed to the increased formation of the metal (II) hydroxide to metal (III) oxyhydroxide, which further escalates the water oxidation reaction [36, 57]. The observed overpotential of MFO ($\eta_{MFO} = 240$ mV) is much lower than the reported $Mn_3O_4$ catalyst modified with transition metals and noble metals [33, 34, 36].

The Tafel slope is an important parameter that describes the relationship between the rate of an electrochemical reaction with the potential and assesses the performance of a given catalyst towards the OER [58–60]. It was reported that the catalyst with the lower Tafel slope shows better catalytic activity for the water oxidation [36, 58, 60, 61]. Figure 7(b) shows the Tafel plots of MO, MCO, and MFO. MO shows a Tafel slope of 163 mV $dec^{-1}$, which is much smaller than the 231 mV $dec^{-1}$ reported by Maruthapandian *et al* [36], and slightly higher than the 126 mV $dec^{-1}$ reported by Debnath *et al*, in the case of $Mn_3O_4$ nano-cubes [61]. The MCO and MFO show a Tafel slope of 149 mV $dec^{-1}$ and 137 mV $dec^{-1}$, respectively. These values are slightly lower than the MO and corroborate the enhanced OER activity in the case of MCO and MFO. Among the prepared catalysts, MFO shows the lower Tafel slope (137 mV $dec^{-1}$) and better catalytic activity for the OER. To investigate the effect of the ECSA on the OER activity of the catalysts, we have estimated the ECSA of the catalysts with the help of double-layer capacitance ($C_{dl}$), obtained from figure 8, and specific capacitance ($C_s$). Among the catalysts, MFO shows the lower ($MFO_{ECSA} = 7.25 \times 10^{-3}$ $cm^2$) ECSA compared to MO ($MO_{ECSA} = 25.5 \times 10^{-3}$ $cm^2$) and MCO ($MCO_{ECSA} = 56.3 \times 10^{-3}$ $cm^2$). Despite a lower ECSA, MFO exhibits better OER activity compared to MO and MCO. This suggests that the enhanced OER activity of MFO could be attributed to electronic effects resulting from the doping of Fe in the pristine catalyst [62].

To further understand the reason for the better OER activity of MFO over MO and MCO catalysts, we calculated the TOF of these catalysts and found that the MFO catalyst (0.0119 $s^{-1}$) possesses a higher TOF in comparison with the MO ($8.20 \times 10^{-4}$ $s^{-1}$) and MCO ($1.08 \times 10^{-3}$ $s^{-1}$) catalysts. It is known that a catalyst with a higher TOF exhibits better performance [48, 49]; a similar trend was observed in the as-synthesized catalysts and MFO shows better activity among them.

Cycle stability is important for the utilization of catalysts for prolonged usage for OER applications. The stability of the as-synthesized catalysts was investigated by performing cyclic voltammetry with a different number of cycles. Figure 9(a) shows the LSV curves of the MFO catalyst collected at an initial cycle, after 100

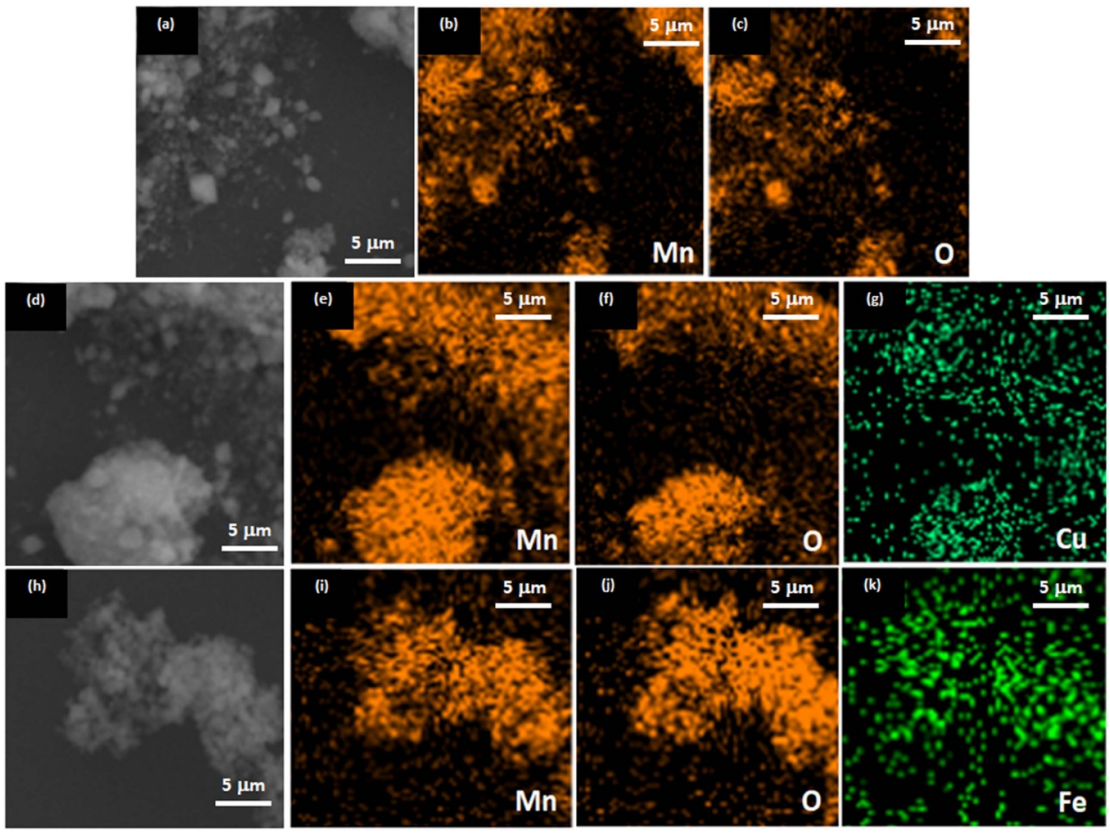


**Figure 5.** Colour-mapping images of (a)–(c) pristine $Mn_3O_4$, (d)–(g) Cu-doped $Mn_3O_4$, and (h)–(k) Fe-doped $Mn_3O_4$ catalysts.

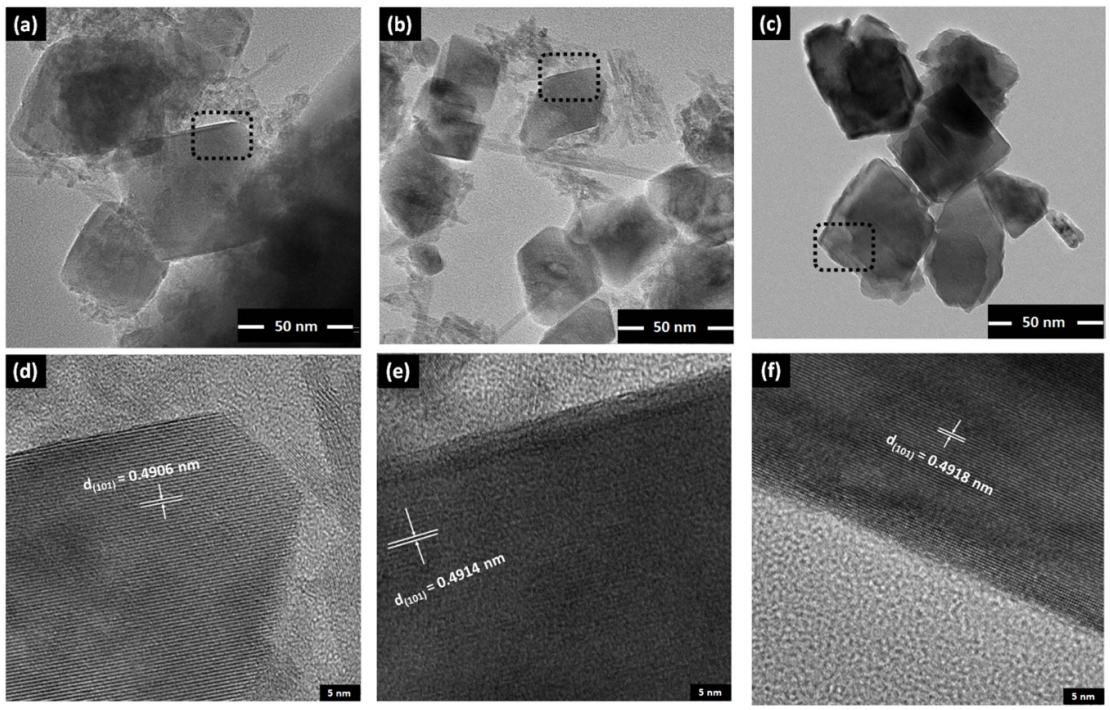


**Figure 6.** Transmission electron micrographs of (a) pristine $Mn_3O_4$, (b) Fe-doped $Mn_3O_4$, and (c) Cu-doped $Mn_3O_4$, and high-resolution transmission electron micrographs of (d) pristine $Mn_3O_4$, (e) Fe-doped $Mn_3O_4$, and (f) Cu-doped $Mn_3O_4$.

cycles, and after 500 cycles. It is evident that the onset potential of the OER is slightly shifted towards higher potential and it is seen that the current density of the MFO is reduced. Figure 9(a) indicates that the onset potential of MFO is not altered up to 500 cycles, whereas it shows a slight decrease in the current density. To

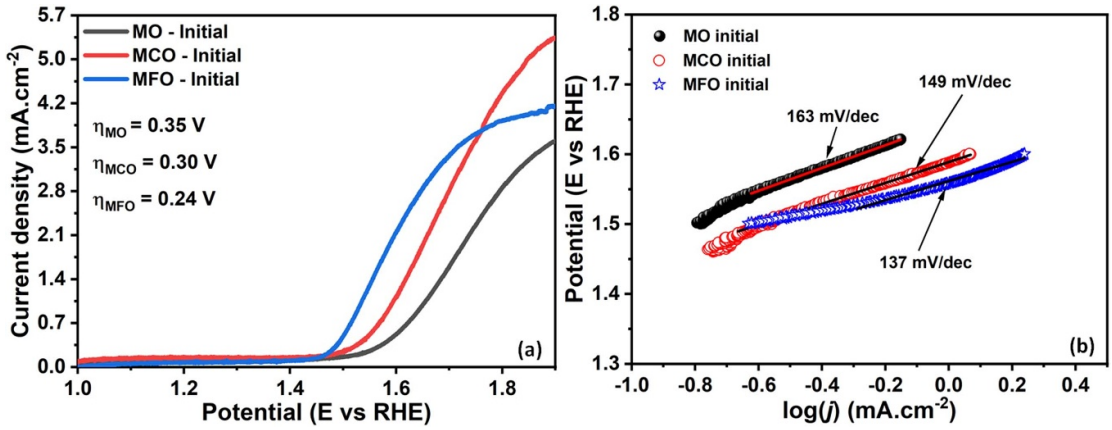


**Figure 7.** (a) Linear sweep voltammetry curves of pristine $Mn_3O_4$, Cu-doped $Mn_3O_4$ (MCO), and Fe-doped $Mn_3O_4$ (MFO). (b) Tafel lines of pristine $Mn_3O_4$, Cu-doped $Mn_3O_4$ (MCO), and Fe-doped $Mn_3O_4$ (MFO).

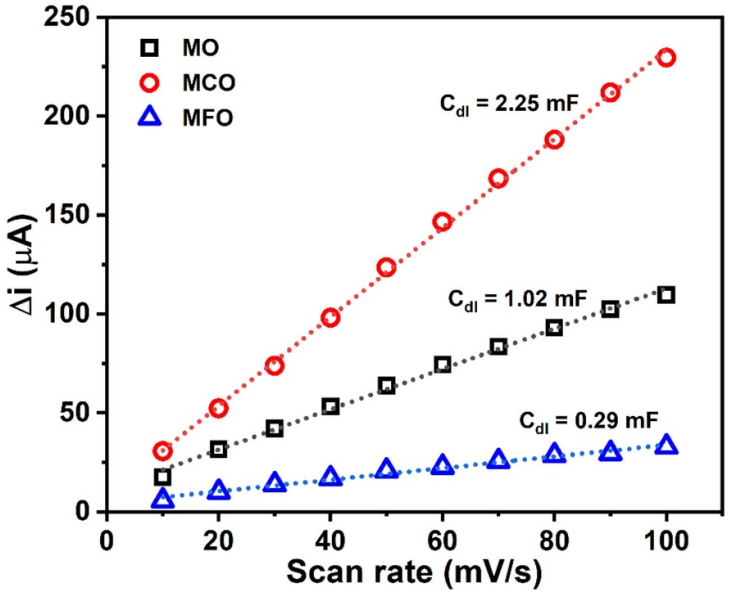


**Figure 8.** Capacitive current as a function of scan rate of pristine $Mn_3O_4$ (MO), Cu-doped $Mn_3O_4$ (MCO), and Fe-doped $Mn_3O_4$ (MFO) catalysts.

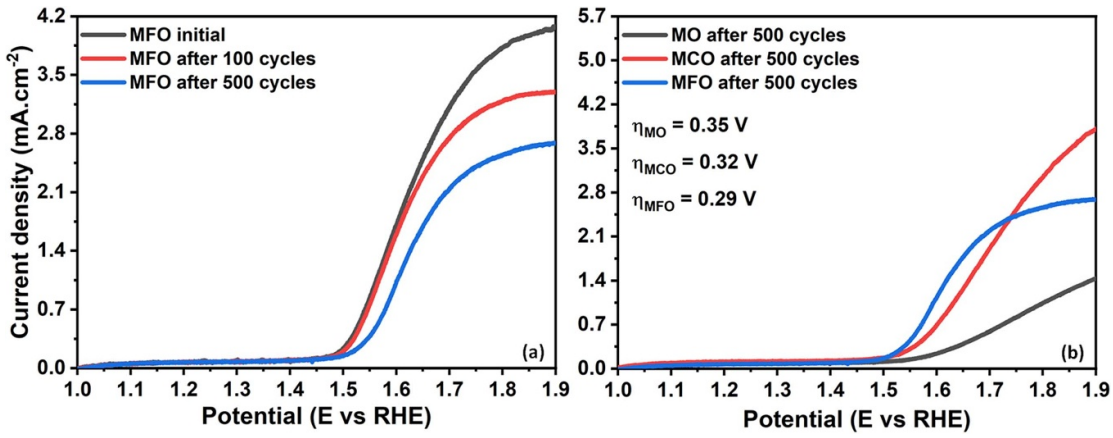


**Figure 9.** (a) Linear sweep voltammetry curves of Fe-doped $Mn_3O_4$ (MFO) collected after a different number of cycles. (b) Linear sweep voltammetry curves of pristine $Mn_3O_4$, Cu-doped $Mn_3O_4$ (MCO), and Fe-doped $Mn_3O_4$ (MFO) catalysts collected after 500 cycles.

compare the cyclic stability of MFO with the other prepared catalysts, we have performed a similar measurement on MO and MCO and the results are shown in the figure 9(b). This indicates that the MFO catalyst shows better activity in comparison with MO and MCO even after 500 cycles. The modifications in the activity of these catalysts could be correlated with the formation of metal oxide and metal-oxyhydroxide during the catalytic activity.

## 5. Conclusions

We successfully synthesized MO and transition metal (Cu and Fe) doped $Mn_3O_4$ with the help of a hydrothermal technique. The phase purity of the as-prepared catalysts was confirmed by the PXRD technique and was further supported with HRTEM studies. A systematic OER study on these catalysts revealed that MFO showed an enhanced catalytic activity over the MO and MCO. The best catalyst, MFO, displayed an overpotential of $\eta_{MFO} = 240$ mV and a Tafel slope of 137 mV $dec^{-1}$. ECSA studies of the MFO revealed that the better OER activity could be due to the electronic effects. The TOF of the MFO was found to be 0.0119 $s^{-1}$, which further supports its better performance. The MFO catalyst exhibits cyclic stability of over 500 cycles. The enhanced catalytic activity of MFO may be attributed to the increased formation of intermediate hydroxides and oxyhydroxides, which further modulate the adsorption-desorption properties of hydroxide or oxygen atoms.

## Data availability statement

All data that support the findings of this study are included within the article (and any supplementary files).

## Acknowledgments

SDR thank the management, VNR VJIET, for providing a vibrant environment for the execution of the current research work. P S and K R K thank Koneru Lakshmaiah Education Foundation (KLEF) for their constant encouragement and support in executing the current work. K R K is also grateful to the Department of Science and Technology (DST), Govt. of India, for the award of the DST-FIST Level-1 (Grant No. SR/FST/PS-1/2018/35) scheme to the Department of Physics, KLEF.

## Conflict of interest

The authors declare that they have no competing financial interests or personal relationships that could have appeared to influence the work reported in this article.

## ORCID iDs

S D Ramarao https://orcid.org/0000-0002-9252-8587
Hitesh Borkar https://orcid.org/0000-0002-6139-4811
Ch Rajesh https://orcid.org/0000-0002-7022-0549

## References

[1] Tahir M, Pan L, Idrees F, Zhang X, Wang L, Zou J J and Wang Z L 2017 Electrocatalytic oxygen evolution reaction for energy conversion and storage: a comprehensive review *Nano Energy* **37** 136–57
[2] Wang Z L, Xu D, Xu J J and Zhang X B 2014 Oxygen electrocatalysts in metal-air batteries: from aqueous to nonaqueous electrolytes *Chem. Soc. Rev.* **43** 7746–86
[3] Höök M and Tang X 2013 Depletion of fossil fuels and anthropogenic climate change—a review *Energy Policy* **52** 797–809
[4] Michaelides E E 2017 A new model for the lifetime of fossil fuel resources *Nat. Resour. Res.* **26** 161–75
[5] Devabhaktuni V, Alam M, Depuru S S S R, Green R C, Nims D and Near C 2013 Solar energy: trends and enabling technologies *Renew. Sustain. Energy Rev.* **19** 555–64
[6] Boudghene Stambouli A and Traversa E 2002 Fuel cells, an alternative to standard sources of energy *Renew. Sustain. Energy Rev.* **6** 295–304
[7] Stambouli A B and Traversa E 2002 Solid oxide fuel cells (SOFCs): a review of an environmentally clean and efficient source of energy *Renew. Sustain. Energy Rev.* **6** 433–55
[8] Abbasi R *et al* 2019 A roadmap to low-cost hydrogen with hydroxide exchange membrane electrolyzers *Adv. Mater.* **31** 1805876
[9] Miller H A, Bouzek K, Hnat J, Loos S, Bernäcker C I, Weißgärber T, Röntzsch L and Meier-Haack J 2020 Green hydrogen from anion exchange membrane water electrolysis: a review of recent developments in critical materials and operating conditions *Sustain. Energy Fuels* **4** 2114–33
[10] Sumboja A, Ge X, Zong Y and Liu Z 2016 Progress in development of flexible metal-air batteries *Funct. Mater. Lett.* **9** 1630001
[11] Han X, Li X, White J, Zhong C, Deng Y, Hu W and Ma T 2018 Metal–air batteries: from static to flow system *Adv. Energy Mater.* **8** 1801396

[12] Zhao S, Yan L, Luo H, Mustain W and Xu H 2018 Recent progress and perspectives of bifunctional oxygen reduction/evolution catalyst development for regenerative anion exchange membrane fuel cells *Nano Energy* **47** 172–98

[13] Suen N T, Hung S F, Quan Q, Zhang N, Xu Y J and Chen H M 2017 Electrocatalysis for the oxygen evolution reaction: recent development and future perspectives *Chem. Soc. Rev.* **46** 337–65

[14] Shi Q, Zhu C, Du D and Lin Y 2019 Robust noble metal-based electrocatalysts for oxygen evolution reaction *Chem. Soc. Rev.* **48** 3181–92

[15] Jamesh M I and Sun X 2018 Recent progress on earth abundant electrocatalysts for oxygen evolution reaction (OER) in alkaline medium to achieve efficient water splitting—a review *J. Power Sources* **400** 31–68

[16] Wang Y, Chen D, Zhang J, Balogun M S, Wang P, Tong Y and Huang Y 2022 Charge relays via dual carbon-actions on nanostructured $BiVO_4$ for high performance photoelectrochemical water splitting *Adv. Funct. Mater.* **32** 2112738

[17] Browne M P, Sofer Z and Pumera M 2019 Layered and two dimensional metal oxides for electrochemical energy conversion *Energy Environ. Sci.* **12** 41–58

[18] Han L, Dong S and Wang E 2016 Transition-metal (Co, Ni, and Fe)-based electrocatalysts for the water oxidation reaction *Adv. Mater.* **28** 9266–91

[19] Feng C, Faheem M B, Fu J, Xiao Y, Li C and Li Y 2020 Fe-based electrocatalysts for oxygen evolution reaction: progress and perspectives *ACS Catal.* **10** 4019–47

[20] Yi H *et al* 2021 Recent advance of transition-metal-based layered double hydroxide nanosheets: synthesis, properties, modification, and electrocatalytic applications *Adv. Energy Mater.* **11** 2002863

[21] Dionigi F, Zhu J, Zeng Z, Merzdorf T, Sarodnik H, Gliech M, Pan L, Li W-X, Greeley J and Strasser P 2021 Intrinsic electrocatalytic activity for oxygen evolution of crystalline 3D-transition metal layered double hydroxides *Angew. Chem.* **133** 14567–78

[22] Ghosh S K 2020 Diversity in the family of manganese oxides at the nanoscale: from fundamentals to applications *ACS Omega* **5** 25493–504

[23] Boucher B, Buhl R and Perrin M 1971 Magnetic structure of $Mn_3O_4$ by neutron diffraction *J. Appl. Phys.* **42** 1615–7

[24] Tian Z Y, Mountapmbeme Kouotou P, Bahlawane N and Tchoua Ngamou P H 2013 Synthesis of the catalytically active $Mn_3O_4$ spinel and its thermal properties *J. Phys. Chem.* C **117** 6218–24

[25] Dong R, Ye Q, Kuang L, Lu X, Zhang Y, Zhang X, Tan G, Wen Y and Wang F 2013 Enhanced supercapacitor performance of $Mn_3O_4$ nanocrystals by doping transition-metal ions *ACS Appl. Mater. Interfaces* **5** 9508–16

[26] Wang J G, Jin D, Zhou R, Li X, Liu X R, Shen C, Xie K, Li B, Kang F and Wei B 2016 Highly flexible graphene/$Mn_3O_4$ nanocomposite membrane as advanced anodes for Li-ion batteries *ACS Nano* **10** 6227–34

[27] Carrillo A J, Serrano D P, Pizarro P and Coronado J M 2015 Improving the thermochemical energy storage performance of the $Mn_2O_3$/$Mn_3O_4$ redox couple by the incorporation of iron *ChemSusChem* **8** 1947–54

[28] Bigiani L, Maccato C, Carraro G, Gasparotto A, Sada C, Comini E and Barreca D 2018 Tailoring vapor-phase fabrication of $Mn_3O_4$ nanosystems: from synthesis to gas-sensing applications *ACS Appl. Nano Mater.* **1** 2962–70

[29] Jain P, Patel K, Jangid A K, Guleria A, Patel S, Pooja D and Kulhari H 2021 Biotinylated $Mn_3O_4$ nanocuboids for targeted delivery of gemcitabine hydrochloride to breast cancer and MRI applications *Int. J. Pharm.* **606** 120895

[30] Ramírez A, Hillebrand P, Stellmach D, May M M, Bogdanoff P and Fiechter S 2014 Evaluation of $MnO_x$, $Mn_2O_3$, and $Mn_3O_4$ electrodeposited films for the oxygen evolution reaction of water *J. Phys. Chem.* C **118** 14073–81

[31] Cho K H, Seo H, Park S, Lee Y H, Lee M Y, Cho N H and Nam K T 2020 Uniform, assembled 4 nm $Mn_3O_4$ nanoparticles as efficient water oxidation electrocatalysts at neutral pH *Adv. Funct. Mater.* **30** 1910424

[32] Rani B J, Ravi G, Yuvakkumar R, Hong S I, Velauthapillai D, Thambidurai M, Dang C and Saravanakumar B 2020 Neutral and alkaline chemical environment dependent synthesis of $Mn_3O_4$ for oxygen evolution reaction (OER) *Mater. Chem. Phys.* **247** 122864

[33] Li Z Y, Liu Z L, Liang J C, Xu C W and Lu X 2014 Facile synthesis of Pd-$Mn_3O_4$/C as high-efficient electrocatalyst for oxygen evolution reaction *J. Mater. Chem.* A **2** 18236–40

[34] Li Z Y, Shi S T, Zhong Q S, Zhang C J and Xu C W 2014 Pt-$Mn_3O_4$/C as efficient electrocatalyst for oxygen evolution reaction in water electrolysis *Electrochim. Acta* **146** 119–24

[35] Nagajyothi P C, Ramaraghavulu R, Munirathnam K, Yoo K and Shim J 2021 One-pot hydrothermal synthesis: enhanced MOR and OER performance using low-cost $Mn_3O_4$ electrocatalyst *Int. J. Hydrog. Energy* **46** 13946–51

[36] Maruthapandian V, Pandiarajan T, Saraswathy V and Muralidharan S 2016 Oxygen evolution catalytic behaviour of Ni doped $Mn_3O_4$ in alkaline medium *RSC Adv.* **6** 48995–9002

[37] Hong J S, Seo H, Lee Y H, Cho K H, Ko C, Park S and Nam K T 2020 Nickel-doping effect on $Mn_3O_4$ nanoparticles for electrochemical water oxidation under neutral condition *Small Methods* **4** 1900733

[38] Huang Q, Zhong X, Zhang Q, Wu X, Jiao M, Chen B, Sheng J and Zhou G 2021 $Co_3O_4$/$Mn_3O_4$ hybrid catalysts with heterointerfaces as bifunctional catalysts for Zn-air batteries *J. Energy Chem.* **68** 679–87

[39] Chutia B, Hussain N, Puzari P, Jampaiah D, Bhargava S K, Matus E V, Ismagilov I Z, Kerzhentsev M and Bharali P 2021 Unraveling the role of $CeO_2$ in stabilization of multivalent Mn species on α-$MnO_2$/$Mn_3O_4$/$CeO_2$/C surface for enhanced electrocatalysis *Energy Fuels* **35** 10756–69

[40] Gao M R, Xu Y F, Jiang J, Zheng Y R and Yu S H 2012 Water oxidation electrocatalyzed by an efficient $Mn_3O_4$/$CoSe_2$ nanocomposite *J. Am. Chem. Soc.* **134** 2930–3

[41] Hu C, Zhang L, Huang Z, Zhu W, Zhao Z J and Gong J 2019 Facet-evolution growth of $Mn_3O_4$@$Co_xMn_{3-x}O_4$ electrocatalysts on Ni foam towards efficient oxygen evolution reaction *J. Catal.* **369** 105–10

[42] Song Y, Liu H, Dong W and Li M 2020 Designed synthesis of hierarchical $Mn_3O_4$@$SnO_2$/$Co_3O_4$ core-shell nanocomposite for efficient electrocatalytic water splitting *Int. J. Hydrog. Energy* **45** 4501–10

[43] Hu C, Zhang L, Zhao Z J, Luo J, Shi J, Huang Z and Gong J 2017 Edge sites with unsaturated coordination on core–shell $Mn_3O_4$@$Mn_xCo_{3-x}O_4$ nanostructures for electrocatalytic water oxidation *Adv. Mater.* **29** 1701820

[44] Fominykh K *et al* 2015 Iron-doped nickel oxide nanocrystals as highly efficient electrocatalysts for alkaline water splitting *ACS Nano* **9** 5180–8

[45] Bau J A, Luber E J and Buriak J M 2015 Oxygen evolution catalyzed by nickel-iron oxide nanocrystals with a nonequilibrium phase *ACS Appl. Mater. Interfaces* **7** 19755–63

[46] Zhou K and Li Y 2012 Catalysis based on nanocrystals with well-defined facets *Angew. Chem., Int. Ed.* **51** 602–13

[47] Jung S, McCrory C C L, Ferrer I M, Peters J C and Jaramillo T F 2016 Benchmarking nanoparticulate metal oxide electrocatalysts for the alkaline water oxidation reaction *J. Mater. Chem.* A **4** 3068–76

[48] Anantharaj S, Karthik P E and Noda S 2021 The significance of properly reporting turnover frequency in electrocatalysis research *Angew. Chem., Int. Ed.* **60** 23051–67

[49] Yin J, Zhou P, An L, Huang L, Shao C, Wang J, Liu H and Xi P 2016 Self-supported nanoporous $NiCo_2O_4$ nanowires with cobalt-nickel layered oxide nanosheets for overall water splitting *Nanoscale* **8** 1390–400
[50] Li G, Tang X, Lou S and Zhou S 2014 Large enhancement of ferromagnetism by Cr doping in $Mn_3O_4$ nanowires *Appl. Phys. Lett.* **104** 173105
[51] Hirai S, Yagi S, Seno A, Fujioka M, Ohno T and Matsuda T 2016 Enhancement of the oxygen evolution reaction in $Mn^{3+}$-based electrocatalysts: correlation between Jahn–Teller distortion and catalytic activity *RSC Adv.* **6** 2019–23
[52] Shannon R D 1976 Revised effective ionic radii and systematic studies of interatomic distances in halides and chalcogenides *Acta Crystallogr.* A **32** 751–67
[53] Patterson A L 1939 The Scherrer formula for x-ray particle size determination *Phys. Rev.* **56** 978–82
[54] Vázquez-Olmos A, Redón R, Rodríguez-Gattorno G, Mata-Zamora M E, Morales-Leal F, Fernández-Osorio A L and Saniger J M 2005 One-step synthesis of $Mn_3O_4$ nanoparticles: structural and magnetic study *J. Colloid Interface Sci.* **291** 175–80
[55] Zhao N, Wang S, Cheng P, Zhang J, Zhang L, Du W and Tang N 2021 Controllable fabrication of $Co_{3-x}Mn_xO_4$ with tunable external $Co^{3+}/Co^{2+}$ ratio for promoted oxygen reduction reaction *Catal. Lett.* **151** 1810–20
[56] Guo C X, Chen S and Lu X 2014 Ethylenediamine-mediated synthesis of $Mn_3O_4$ nano-octahedrons and their performance as electrocatalysts for the oxygen evolution reaction *Nanoscale* **6** 10896–901
[57] Kim K H, Zheng J Y, Shin W and Kang Y S 2012 Preparation of dendritic NiFe films by electrodeposition for oxygen evolution *RSC Adv.* **2** 4759–67
[58] Najafpour M M, Renger G, Hołyńska M, Moghaddam A N, Aro E M, Carpentier R, Nishihara H, Eaton-Rye J J, Shen J R and Allakhverdiev S I 2016 Manganese compounds as water-oxidizing catalysts: from the natural water-oxidizing complex to nanosized manganese oxide structures *Chem. Rev.* **116** 2886–936
[59] Huynh M, Shi C, Billinge S J L and Nocera D G 2015 Nature of activated manganese oxide for oxygen evolution *J. Am. Chem. Soc.* **137** 14887–904
[60] Fang Y H and Liu Z P 2010 Mechanism and Tafel lines of electro-oxidation of water to oxygen on $RuO_2$(110) *J. Am. Chem. Soc.* **132** 18214–22
[61] Debnath B, Kumar A, Salunke H G and Bhattacharyya S 2017 Enhancing multifunctionality through secondary phase inclusion by self-assembly of $Mn_3O_4$ nanostructures with superior exchange anisotropy and oxygen evolution activity *J. Phys. Chem.* C **121** 25594–602
[62] Sarma S C, Mishra V, Ann Mary K A, Roy S and Peter S C 2018 'Inverse strain effect in atomic scale'—enhanced hydrogen evolution activity and durability in Cu-substituted palladseite *ACS Energy Lett.* **3** 3008–14